J. Fluid Mech. (2006), *vol.* 556, *pp.* 217–226. © 2006 Cambridge University Press
doi:10.1017/S0022112006009505 Printed in the United Kingdom

The effects of gravity on the capillary instability in tubes

By VIRGINIE DUCLAUX[1], CHRISTOPHE CLANET[1] AND DAVID QUÉRÉ[2]

[1]IRPHE, UMR 6594, 49 rue F. Joliot-Curie, BP 146, 13384 Marseille, France
[2]Laboratoire de Physique de la Matière Condensée, FRE 2844 du CNRS, Collège de France, 75231 Paris Cedex 05, France

(Received 24 October 2005 and in revised form 14 February 2006)

We study the capillary instability of a liquid film (thickness h_0) coating a horizontal cylindrical tube (radius R_0). We show experimentally that the instability only occurs if $h_0/R_0 > 0.3(R_0/a)^2$, where a is the capillary length. If this criterion is not fulfilled, the liquid film does not destabilize into an array of drops, owing to the gravitational drainage.

1. Introduction

The capillary instability of cylindrical liquid interfaces is a classical topic of interfacial science (Savart 1833; Plateau 1873; Rayleigh 1892; Chandrasekhar 1961; Eggers 1997). Three examples are displayed in figure 1: a liquid jet (figure 1*a*), a liquid film coating a fibre (figure 1*b*) and a liquid film deposited on the inner wall of a tube (figure 1*c*). In each case, the image at the top presents the initial situation and the image at the bottom the shape of the interface after a time τ characterizing the instability.

Introducing the fluid properties (Newtonian liquid with density ρ, surface tension σ, dynamic viscosity μ), the different scaling laws for τ are summarized in table 1, depending on the Reynolds number (Johnson *et al.* 1991). R_i stands for the initial radius of the liquid–air interface and h_0 for the film thickness. In the case of a tube of radius R_0, we have $R_i = R_0 - h_0$.

Here, we study the effect of gravity on the capillary instability in tubes (figure 1*c*) in the 'viscous regime' ($Re \ll 1$) and show how it can affect and even suppress the instability.

2. Experimental setup

The experimental setup is presented in figure 2(*a*). A liquid slug of length L is first introduced into a horizontal glass tube. We only use wetting liquids (silicone oils and glycerol 98 %) whose characteristics are displayed in table 2. The last column of the table gives the capillary length $a \equiv \sqrt{\sigma/\rho g}$. The tube radius R_0 ranges from 150 μm to 1.5 mm.

Once inserted, the liquid slug is pushed by air at a velocity U, using a syringe pump. As it moves, it deposits a film of thickness h_0 on the tube wall. The relative thickness h_0/R_0 is fixed by the capillary number $Ca \equiv \mu U/\sigma$. The relation $h_0/R_0(Ca)$ was

https://doi.org/10.1017/S0022112006009505 Published online by Cambridge University Press

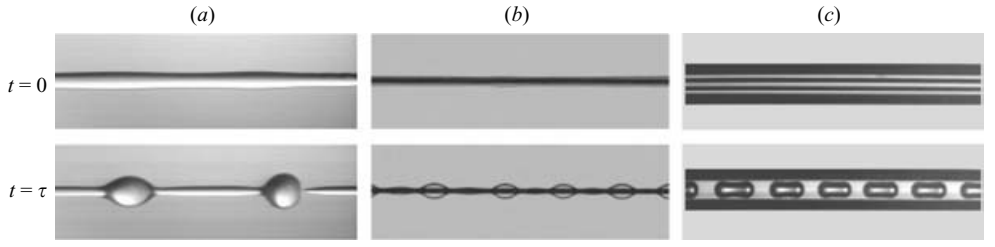


FIGURE 1. Capillary instability of cylindrical interfaces: (*a*) liquid jet, (*b*) liquid film on a fibre, (*c*) liquid film in a tube.

	Jet	Fibre	Tube
$Re \gg 1$	$\tau \sim \sqrt{\rho R_i^3/\sigma}$	$\tau \sim \sqrt{\rho R_i^4/(\sigma h_0)}$	$\tau \sim \sqrt{\rho R_i^4/(\sigma h_0)}$
$Re \ll 1$	$\tau \sim \mu R_i/\sigma$	$\tau \sim \mu R_i^4/(\sigma h_0^3)$	$\tau \sim \mu R_i^4/(\sigma h_0^3)$

TABLE 1. Scaling for the characteristic time τ of the capillary instability for the three different cases displayed in figure 1. For the jet, R_i is the jet radius. For the fibre $R_i = R_0 + h_0$ where R_0 is the fibre radius and h_0 the film thickness. For the tube $R_i = R_0 - h_0$ where R_0 is the inner tube radius and h_0 the film thickness.

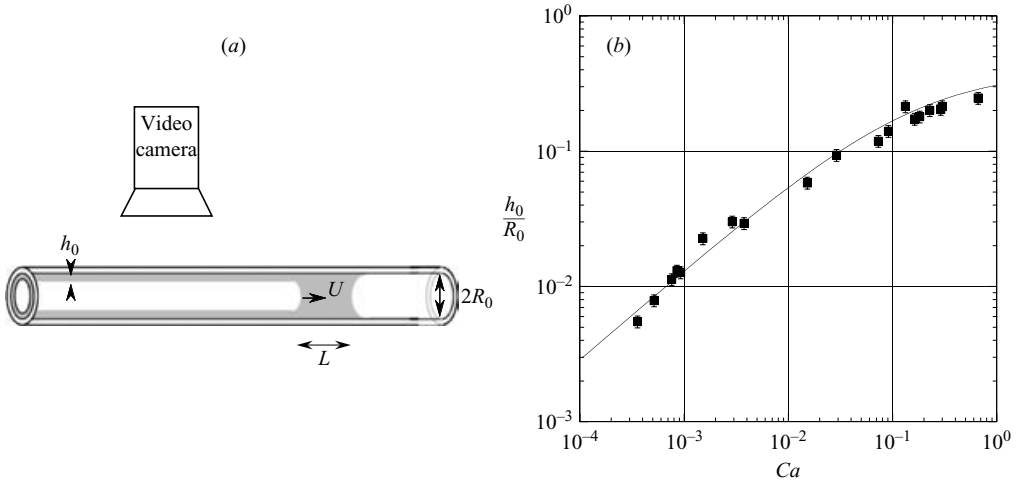


FIGURE 2. (*a*) Experimental setup. (*b*) Evolution of the relative film thickness h_0/R_0 as a function of the capillary number Ca (the continuous line is equation (2.1) and the symbols correspond to our measurements).

Liquid	ρ (kg m^{-3})	μ (kg m^{-1} s^{-1})	σ (kg s^{-2})	a (m)
SO V100	952	0.1	0.0225	$1.6\,10^{-3}$
SO V1000	965	1	0.0225	$1.5\,10^{-3}$
SO V12500	965	12.5	0.0225	$1.5\,10^{-3}$
Glycerol 98 %	1260	0.9	0.063	$2.25\,10^{-3}$

TABLE 2. Physical properties of the different Newtonian liquids (at 25 °C). SO is silicone oil.

https://doi.org/10.1017/S0022112006009505 Published online by Cambridge University Press

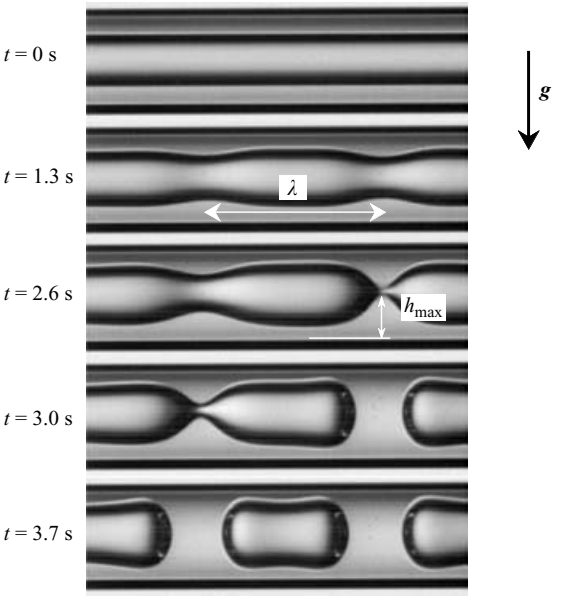


FIGURE 3. Chronophotography of the capillary instability visualized from the side ($R_0 = 420\,\mu$m, $h_0/R_0 = 0.35$, SO V1000). The corresponding characteristic time is $\tau = 1$ s.

experimentally determined by Taylor (1961), and found to obey the law (Aussillous & Quéré 2000):

$$\frac{h_0}{R_0} = \frac{1.34\,Ca^{2/3}}{1 + 3.35\,Ca^{2/3}}. \tag{2.1}$$

This equation extends the small-capillary-number limit derived theoretically by Bretherton (1961) and applies as long as inertia is negligible. We checked the accuracy of this relation by measuring the slug length L as it moves, and deducing the thickness from mass conservation. The film thickness is given in figure 2(*b*) as a function of the capillary number and compared to equation (2.1) (continuous line). This comparison shows that within 10 %, equation (2.1) does predict the measured thickness.

After the film deposition, the interface generally undergoes a varicose-like instability (Rayleigh 1902), as shown in figure 3. This deformation is observed with a video camera under a binocular lens. We measured the wavelength λ and the dynamics of the deformation $h_{\max}(t)$, where $h_{\max}$ is the maximum film thickness (see figure 3). In the example of figure 3, we find $\lambda/R_i \approx 8$, and it takes about 3 s for the interface to form plugs. The characteristic time τ of the instability can be evaluated using the expression for the most unstable mode (see § 4) $\tau \equiv 12\mu R_i^4/(\sigma h_0^3) \approx 1$ s.

3. Results

3.1. *When the capillary instability does not occur*

The first striking observation is that the capillary instability is not always observed: this is shown in figure 4(*a*) where we present side and top views of the interface for different thicknesses (at a time $t > \tau$) in the same tube ($R_0 = 420\,\mu$m) and with the same liquid.

(i) For $h_0/R_0 = 0.35$ (figure 4*a*(i)), the instability does occur and both views present a top/bottom symmetry: the phenomenon is axisymmetric.

https://doi.org/10.1017/S0022112006009505 Published online by Cambridge University Press

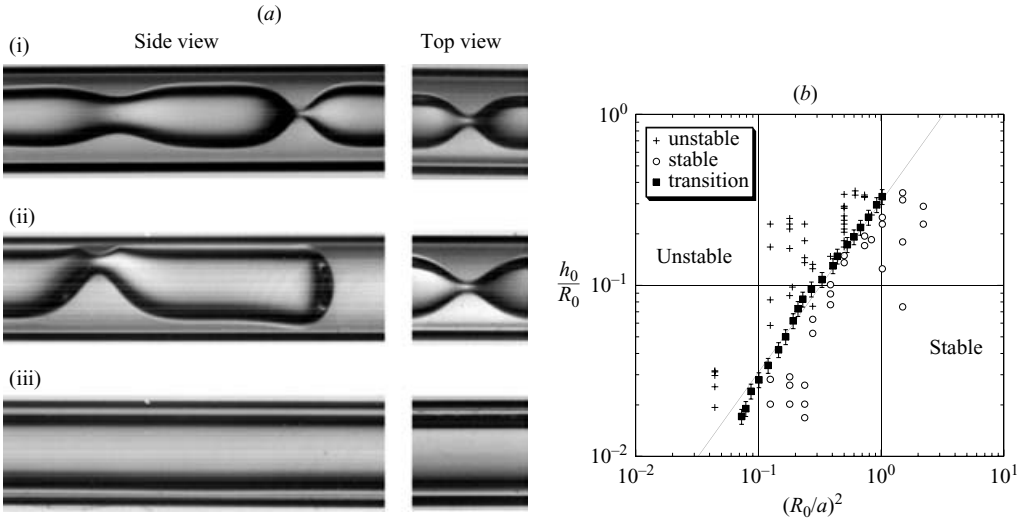


FIGURE 4. Experimental results concerning the transition. (*a*) Side and top views of the interface obtained at $t \gg \tau$ in the same tube ($R_0 = 420\,\mu\text{m}$), with the same silicone oil (V1000) but different thicknesses: (i) $h_0/R_0 = 0.35$ ($t = 2.5\,\text{s}$, $\tau = 1\,\text{s}$), (ii) $h_0/R_0 = 0.19$ ($t = 103\,\text{s}$, $\tau = 14\,\text{s}$) (iii) $h_0/R_0 = 0.034$ ($t = 10000\,\text{s}$, $\tau = 5075\,\text{s}$). (*b*) Transition between stable and unstable interfaces in the plane $[h_0/R_0; (R_0/a)^2]$. For clarity, the errors bars have only been shown on the square symbols, but they are similar in all experiments. The continuous line represents the function $h_0/R_0 = 0.3(R_0/a)^2$.

(ii) For $h_0/R_0 = 0.19$ (figure 4*a*(ii)), the instability occurs but the side view reveals that the phenomenon is no longer axisymmetric: the instability grows from the bottom. We call this regime 'transition' from now on.

(iii) For $h_0/R_0 = 0.03$ (figure 4*a*(iii)), the instability is never observed. In this case, our video camera enables us to record images only up to $t = 10000\,\text{s}$, but the situation remains much longer.

The 'phase diagram' for the state of the interface is presented in figure 4(*b*), where we summarize the results obtained in different tubes with different liquids. In this figure, the relative thickness h_0/R_0 is plotted as a function of the square of the reduced radius $(R_0/a)^2$. We observe that the instability only occurs if $h_0/R_0 > 0.3(R_0/a)^2$ (continuous line).

3.2. *When the capillary instability occurs*

The classical theory of the capillary instability of a cylindrical interface predicts an exponential growth of a varicose deformation of wavelength λ if $\lambda > 2\pi R_i$ (Plateau 1873; Rayleigh 1902; Chandrasekhar 1961). The most unstable wavelength is $\lambda_{th} \equiv 2\pi\sqrt{2}R_i$ with a corresponding growth time $\tau_{th} = 12\mu R_i^4/(\sigma h_0^3)$. The latter expression holds provided the Reynolds number in the film remains smaller than unity, $Re \equiv \rho u h_0/\mu \ll 1$, where u is the typical velocity of the flow.

We present in figure 5(*a*) the evolution of the observed wavelength λ as a function of the interface radius R_i, for different liquids. Ten wavelengths were measured for each experiment to get an accurate mean value. The expected theoretical value is shown by the thick solid line. We observe that the wavelength converges toward the theoretical value for 'small' R_i. When the interface radius becomes of the order of 1 mm, the wavelength increases more than expected by the theory. This tendency is

https://doi.org/10.1017/S0022112006009505 Published online by Cambridge University Press

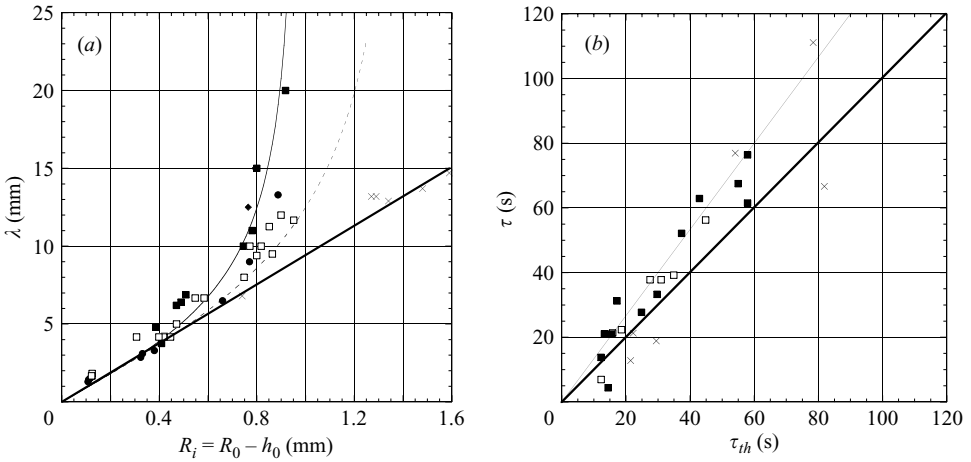


FIGURE 5. (*a*) Evolution of the wavelength λ as a function of the interface radius R_i for different liquids: ■, V100; ●, V1000; ◆, V12500; □, glycerol; ×, experiments by Goldsmith & Mason (1963). The thick continuous line is the classical result $\lambda = 2\pi\sqrt{2}R_i$, the thin continuous line and the dashed line respectively represent the curves $\lambda = 2\pi\sqrt{2}R_i/\sqrt{1-2.5Bo^2}$ for the silicone oils and the glycerol. (*b*) Comparison between the measured characteristic time τ and the theoretical expression $\tau_{th} \equiv 12\mu R_i^4/(\sigma h_0^3)$ for different liquids: ■ V100, □ V1000, × Experiments by Goldsmith & Mason (1963). The thick continuous line stands for the theoretical value and the thin continuous line for the best fit.

more pronounced for silicone oils than for glycerol. Experiments by Goldsmith & Mason (1963) are reported in figure 5(*a*). In their system the influence of gravity has been minimized by matching the densities of the core and annulus fluids. The wavelengths they measure are always very close to the expected theoretical values. This suggests that the deviation observed in our measurements could be due to gravity. The thin continuous and dashed lines represent the function $\lambda = 2\pi\sqrt{2}R_i/\sqrt{1-2.5Bo^2}$, with $Bo \equiv R_i/a$ the Bond number, for silicone oils and glycerine respectively. This fitting function (which will be justified in § 4.2) suggests that the wavelength diverges when the interface radius tends to the capillary length.

The measured growth rate $1/\tau$ is the slope of the curve $\ln[h_{\max}(t)]$ extracted from the linear part of the growth. This time is smaller than the time to completely form the liquid plug. τ is plotted in figure 5(*b*) as a function of τ_{th}, the value expected for the most unstable mode. In these experiments the tube radius was constant ($R = 0.4$ mm) and both the viscosity and the thickness were varied. A linearity between τ and τ_{th} is found but the measured values are systematically above the theoretical ones (thick line). A best fit of the data (thin line) suggests that $\tau \approx 1.34\tau_{th}$. The experiments by Goldsmith & Mason (1963) also give the same result, with a larger dispersion.

3.3. *Evidence for drainage*

In order to show the gravitational drainage, we visualize the interface using a video camera aligned along the axis of symmetry z of the tube. The resulting pictures are displayed in figure 6 for an unstable interface (*a*) and for an interface in the transition region (*b*). In both cases, drainage can be observed, but it is much more pronounced

https://doi.org/10.1017/S0022112006009505 Published online by Cambridge University Press

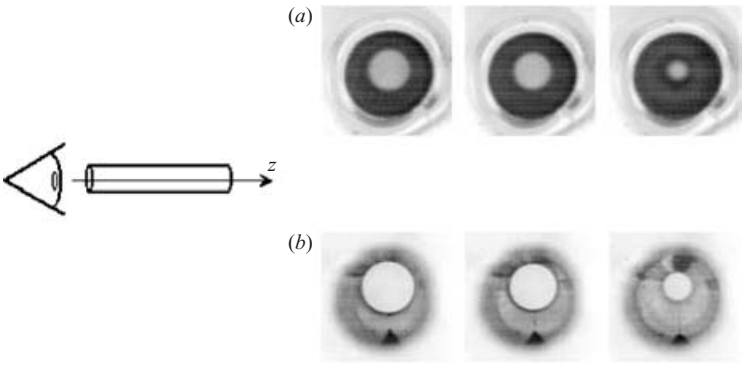


FIGURE 6. Evidence for drainage: (*a*) unstable interface observed at three different times in a tube of radius 0.69 mm with $h_0/R_0 \sim 0.34$; (*b*) unstable interface in the transition regime, observed at three different times in a tube of radius 0.6 mm with $h_0/R_0 \sim 0.07$.

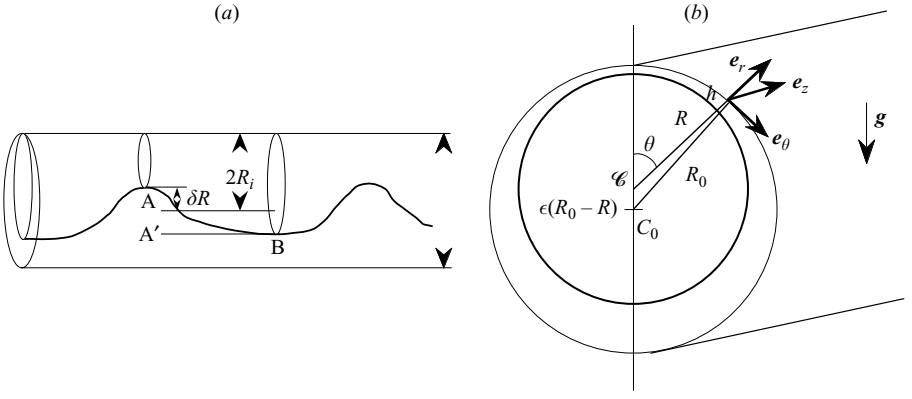


FIGURE 7. Notation used for the theoretical description; (*a*) side view; (*b*) cross-section.

in the transition region. Figure 6 also shows that despite the drainage, the interface always remains circular.

4. Model

The theoretical description of the interface evolution is discussed using the conventions shown in figure 7(*a*): the liquid/air interface has a radius $R(z,t)$ and a centre C which moves with time vertically from its initial location C_0 (centre of the tube) to $R_0 - R$. We use cylindrical coordinates centred at C and denote $\epsilon(R_0 - R)$ as the excentricity of the interface with respect to the tube.

4.1. *Qualitative arguments*

A criterion for the transition can be obtained by comparing the characteristic time of the instability $\tau \sim \mu R_i^4/(\sigma h_0^3)$ to the characteristic time of drainage $\tau_d \sim \mu R_i/(\rho g h_0^2)$. The latter is simply the time required for a vertical viscous film of thickness h_0 to fall under its weight a distance R_i. The ratio τ/τ_d is written

$$\frac{\tau}{\tau_d} \sim \frac{R_i^3}{a^2 h_0} \tag{4.1}$$

https://doi.org/10.1017/S0022112006009505 Published online by Cambridge University Press

where $a \equiv \sqrt{\sigma/(\rho g)}$ is the capillary length. The instability is expected to occur in the limit $\tau/\tau_d \ll 1$ and to be affected by gravity when $\tau/\tau_d \gg 1$: then a liquid particle falls faster under gravity than it is raised by capillarity, so that one might expect the instability to be suppressed. For $R_i \sim R_0$, this criterion is: $h_0/R_0 < (R_0/a)^2$, in good agreement with the results shown in figure 4(*b*).

A physical argument can also be proposed to understand the increase of the wavelength due to gravity. Using Laplace and hydrostatic equations to evaluate the pressure difference between A' and B (isolevel points in figure 7*a*) leads to

$$P_B - P_{A'} = 2\delta R \frac{\sigma}{R_i^2}\left[1 - \left(\frac{R_i}{a}\right)^2 - (kR_i)^2\right]. \tag{4.2}$$

Since the instability only develops if $P_B > P_{A'}$, we deduce that the wavelength must satisfy the relation: $\lambda > 2\pi R_i/\sqrt{1 - Bo^2}$, which diverges when the Bond number approaches unity.

4.2. *Theoretical approach to the transition*

The description of the interface motion is classically based on mass conservation, Stokes equation and boundary conditions at the interface, using lubrication approximations ($\partial/\partial r \gg \partial/r\partial\theta$, $\partial/\partial r \gg \partial/\partial z$) and small slope limit ($\partial h/\partial z \ll 1$ and $\partial h/r\partial\theta \ll 1$). Using the conventions of figure 7, mass conservation is written

$$\frac{\partial(Rh)}{\partial t} = -\frac{\partial(h\bar{u}_\theta)}{\partial\theta} - \frac{\partial(Rh\bar{u}_z)}{\partial z} \tag{4.3}$$

where $\bar{u}_\theta$ and $\bar{u}_z$ stand for the mean velocities in the film along the $\boldsymbol{e}_\theta$ and $\boldsymbol{e}_z$ directions. Stokes' equation expresses the balance between pressure gradient, gravity and viscous force acting on a liquid element.

$$-\nabla p + \rho \boldsymbol{g} + \mu \Delta \boldsymbol{u} = 0 \tag{4.4}$$

(i) Along $\boldsymbol{e}_r$, this force balance reduces to $\partial p/\partial r = -\rho g \cos\theta$, which yields

$$p = p_0 - \sigma\mathscr{C} - \rho g \cos\theta (r - R) \tag{4.5}$$

where p_0 is the atmospheric pressure and $\mathscr{C}$ is the total curvature.

(ii) Along $\boldsymbol{e}_\theta$, and in the thin-film limit, equation (4.4) leads to $\mu \mathrm{d}^2 u_\theta/\mathrm{d}r^2 = \partial p/R\partial\theta - \rho g \sin\theta$. This equation can be integrated twice (using the no-slip condition at the wall and continuity of stress at the interface), which gives the mean velocity along $\boldsymbol{e}_\theta$:

$$\bar{u}_\theta = \frac{h^2}{3\mu}\left(\rho g \sin\theta + \frac{\sigma}{R}\frac{\partial\mathscr{C}}{\partial\theta}\right). \tag{4.6}$$

(iii) Along $\boldsymbol{e}_z$, Stokes' equation can be treated in the same way as along the $\boldsymbol{e}_\theta$-direction which provides the mean velocity $\bar{u}_z$:

$$\bar{u}_z = -\frac{h^2}{3\mu}\left(\rho g \cos\theta \frac{\partial R}{\partial z} - \sigma\frac{\partial\mathscr{C}}{\partial z}\right). \tag{4.7}$$

The next step is to evaluate the total curvature of the interface $\mathscr{C}(z, \theta, t)$. As sketched in figure 7, and confirmed in figure 6, we assume that the interface always remains circular. This assumption holds provided surface tension dominates viscous and gravity effects, that is, at small capillary and Bond numbers ($Ca \equiv \mu\bar{u}_\theta/\sigma \ll 1$; $Bo \equiv R_i/a < 1$), which is the case in this study. This condition leads to the expression

https://doi.org/10.1017/S0022112006009505 Published online by Cambridge University Press

for the total curvature, which in the small-slope limits

$$\mathscr{C} \approx \frac{1}{R} + \frac{\partial^2 h}{\partial z^2}. \tag{4.8}$$

The circular condition also provides a geometrical relation between h and R which reduces in the thin-film limit ($h/R \ll 1$) to

$$h(z,\theta,t) = [R_0 - R(z,t)][1 - \epsilon(t)\cos\theta]. \tag{4.9}$$

The last step is to impose a varicose-like perturbation to the interface $h(z,\theta,t) = [R_0 - R_i(1 + \delta e^{i(kz-\omega t)})][1 - \epsilon(t)\cos\theta]$, where R_i is the initial radius of the interface and δ is a small parameter. At the leading order in δ and ϵ, the different terms of equation (4.3) take the form

$$\frac{\partial(Rh)}{\partial t} \approx R_i h_0 \left[-\cos\theta \frac{\partial \epsilon}{\partial t} + i\omega \frac{R_i}{h_0} \delta e^{i(kz-\omega t)} \right], \tag{4.10}$$

$$\frac{\partial(h\bar{u}_\theta)}{\partial \theta} \approx \frac{\rho g h_0^3}{3\mu} \cos\theta \left[1 - 3\frac{R_i}{h_0} \delta e^{i(kz-\omega t)} \right], \tag{4.11}$$

$$\frac{\partial(Rh\bar{u}_z)}{\partial z} \approx \frac{R_i^2 h_0^3 k^2}{3\mu} \delta e^{i(kz-\omega t)} \left(\frac{\sigma}{R_i^2} + \rho g \cos\theta - \sigma k^2 \right). \tag{4.12}$$

The mass conservation (4.3) leads to an equation for $\epsilon(t)$:

$$\frac{d\epsilon}{dt} = \frac{\rho g h_0^2}{3\mu R_i} \tag{4.13}$$

and to the dispersion relation

$$-i\omega = \frac{\sigma h_0^3}{3\mu R_i^4} \left[(kR_i)^2 (1 + Bo^2 \cos\theta - (kR_i)^2) - 3Bo^2 \frac{R_i}{h_0} \cos\theta \right]. \tag{4.14}$$

Equation (4.13) describes the dynamics of the drainage and provides an estimate of its characteristic time $\tau_d \approx 3\mu R_i/(\rho g h_0^2)$. On the other hand, the dispersion relation (4.14) can be interpreted as follows:

(i) In the zero-gravity limit ($Bo \ll 1$, $Bo^2 R_i/h_0 \ll 1$), equation (4.14) reduces to the classical expression (Goren 1961)

$$-i\omega = \frac{\sigma h_0^3}{3\mu R_i^4} (kR_i)^2 [1 - (kR_i)^2]. \tag{4.15}$$

This dispersion relation implies that the initial perturbation will grow exponentially in time if $kR_i < 1$. The fastest mode is $kR_i = 1/\sqrt{2}$ and the corresponding growth rate $(-i\omega)_{max} = \sigma h_0^3/(12\mu R_i^4)$.

(ii) For finite gravity ($Bo \ll 1$, $Bo^2 R_i/h_0 = O(1)$), the first effect predicted by equation (4.14) is a reduction of the growth rate in the upper part of the tube ($\cos\theta > 0$) and its enhancement in the lower part ($\cos\theta < 0$). In this limit, the wavelength of the fastest mode is not affected by gravity. This effect is indeed observed experimentally in the transition region (see figure 4).

(iii) When the Bond number approaches unity, the wavelength of the fastest mode is affected. If we focus on the lower part of the tube we find $\lambda_{max} = 2\pi\sqrt{2}R_i/\sqrt{1 - Bo^2}$. The wavelength thus increases owing to the effect of gravity. The divergence in $1/\sqrt{1 - Bo^2}$ is shown in figure 5. Experimentally, the divergence is slightly faster since we find that $1/\sqrt{1 - 2.5Bo^2}$ agrees better with our measurements.

https://doi.org/10.1017/S0022112006009505 Published online by Cambridge University Press

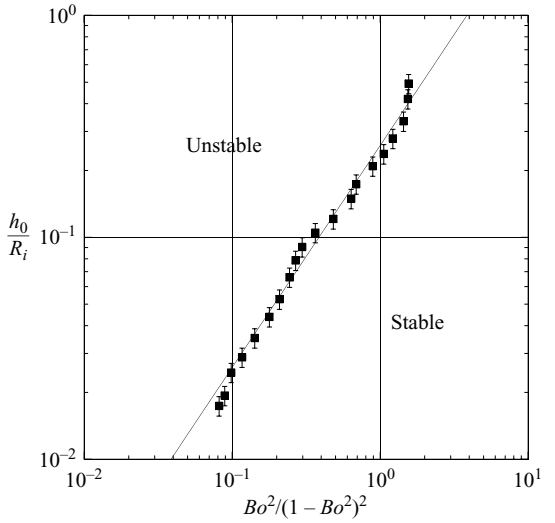


FIGURE 8. Transition between stable and unstable interfaces in the plane $[h_0/R_i; Bo^2/(1-Bo^2)^2]$: ■, experimental data. The continuous line is the best linear fit: $h_0/R_i = 0.26Bo^2/(1-Bo^2)^2$.

(iv) Finally, with the constraint of a circular interface, the instability develops if the interface is unstable for all θ. The capillary instability is thus suppressed by gravity as soon as the upper part becomes stable. According to equation (4.14) this happens for $h_0/R_i \geqslant 12Bo^2/(1-Bo^2)^2$. This criterion is compared to our experimental results in figure 8. The linearity between h_0/R_i and $Bo^2/(1-Bo^2)^2$ is almost satisfied but the prefactor is only 0.26.

Although the model explains several experimental observations (evolution of the wavelength, preferential growth at the bottom, threshold for the instability), it fails in predicting the correct numerical factors.

5. Conclusion

We have studied the effect of gravity on the capillary instability in tubes at low Reynolds numbers. We have shown that the classical results are recovered provided that gravity is negligible ($Bo \ll 1, Bo^2 R_i/h_0 \ll 1$). When gravity is increased ($Bo \ll 1, Bo^2 R_i/h_0 = O(1)$) the wavelength is not affected but the instability develops faster in the lower part of the tube. Finally, when the Bond number approaches one, the wavelength increases. But a main result of the study is that the capillary instability is screened by gravity effects: thin films drain towards the bottom of the tube faster than they develop the instability. This result can be compared to what is observed for films flowing on vertical curved objects – such as tubes or fibres. Then, the instability can generate a 'saturation' of the instability, that is, prevent the drops from developing, provided that the film thickness is smaller than the critical thickness R^3/a^2 (Quéré 1990: Chang 1999). The origin of this effect is quite different, but the physical ingredients being the same, it is logical to find a similar scaling for the critical thickness.

We are grateful to Professor Marc Fermigier from ESPCI for his contribution in figure 1.

https://doi.org/10.1017/S0022112006009505 Published online by Cambridge University Press

REFERENCES

Aussillous, P. & Quéré, D. 2000 Quick deposition of a fluid on the wall of a tube. *Phys. Fluids* **12**, 2367–2371.

Bretherton, F. P. 1961 The motion of long bubbles in tubes. *J. Fluid Mech.* **10**, 166–188.

Chandrasekhar, S. 1961 *Hydrodynamic and Hydromagnetic Stability*. Dover.

Chang, H.-C. & Demekhin, E. A. 1999 Mechanism for drop formation on a coated vertical fibre. *J. Fluid Mech.* **380**, 233–255.

Chauhan, A., Maldarelli, C., Rumschitzki, D. & Papageorgiou, D. T. 2003 An experimental investigation of the convective instability of a jet. *Chem. Engng Sci.* **58**, 2421–2432.

Eggers, J. 1997 Nonlinear dynamics and breakup of free-surface flows. *Rev. Mod. Phys.* **69**, 865–930.

Goldsmith, H. L. & Mason, S. G. 1963 The flow of suspensions through tubes; II. Single large bubbles. *J. Colloid Sci.* **18**, 237–261.

Goren, S. L. 1961 The instability of an annular thread of fluid. *J. Fluid Mech.* **12**, 309–319.

Johnson, M., Kamm, R., Ho, L. W., Shapiro, A. & Pedley, T. J. 1991 The nonlinear growth of surface-tension-driven instabilities of a thin annular film. *J. Fluid Mech.* **233**, 141–156.

Plateau, J. 1873 *Statique Expérimentale et Théorique des Liquides*. Gauthier-Villars.

Quéré, D. 1990 Thin films flowing on vertical fibers. *Europhys. Lett.* **13**, 721–726.

Rayleigh, Lord 1892 On the instability of cylindrical fluid surfaces. *Phil. Mag.* **34**, 177–180.

Rayleigh, Lord 1902 On the instability of cylindrical fluid surfaces. In *Scientific Papers*, vol. 3, pp. 594–596. Cambridge University Press.

Savart, F. 1833 Mémoire sur la constitution des veines liquides lancées par des orifices circulaires en mince paroi. *Ann. de Chim.* **53**, 337–386.

Taylor, G. I. 1961 Deposition of a viscous fluid on the wall of a tube. *J. Fluid Mech.* **10**, 161–165.

https://doi.org/10.1017/S0022112006009505 Published online by Cambridge University Press